Received 3 March 2023; revised 7 July 2023; accepted 10 July 2023. Date of publication 14 July 2023; date of current version 2 August 2023.

*Digital Object Identifier 10.1109/OJAP.2023.3295390*

# Antenna Design for the Arctic Weather Satellite Microwave Sounder

**ROLAND ALBERS[1], ANDERS EMRICH[2], AND AXEL MURK[1]**

[1]Institute of Applied Physics, Bern University, 3012 Bern, Switzerland

[2]AAC Omnisys, 421 32 Västra Frölunda, Sweden

CORRESPONDING AUTHOR: R. ALBERS (e-mail: roland.albers@unibe.ch)

**ABSTRACT** The Arctic Weather Satellite (AWS) is a prototype mission for an operational constellation of microwave sounders, complimenting existing meteorological sounders. The AWS is a microsatellite with a single cross-track scanning radiometer operating in the 54, 89, 183 and 325 GHz bands. Due to the small platform size, the core design focus of the radiometer's quasi-optics is less complexity and a more compact setup than comparable spaceborne microwave sounders. To achieve this, the instrument utilises a splitblock feedarray which directly illuminates the off-axis parabolic scanning reflector. A secondary parabolic reflector is used to couple into a wedge-shaped load which is used for calibration in combination with cold sky measurements. The main challenge for instrument performance is that only one of the four horns can be located in the focus of the scanning reflector. Consequently, scan angle dependent spillover variations and beam asymmetries can occur. This paper details the simulation and optimisation efforts of the quasi-optics to minimise the aforementioned effects.

**INDEX TERMS** Antennas, millimeter-wave (mm-wave), satellite, splitblock, quasi-optics.

## I. MISSION BACKGROUND

MICROWAVE sounders are the most impactful contributors to numerical weather prediction (NWP) [1]. Typically, operational microwave sounders are launched as part of a collection of meteorological instruments on a large satellite platform which restricts both the number of sounders operating concurrently and the rate at which they are replaced due to the slow and costly nature of such major missions. However, there is a need for more frequent measurements in the microwave frequency range, specifically in the 50, 89 and 183 GHz bands [2]. While geostationary satellites offer continuous (but not global) measurements, they are limited in their resolution which is an important driver for NWP due to the height of the orbit and cannot view the high latitudes. Sun-synchronous orbits (SSO) are used by the major meteorological missions to benefit from increased resolution (from being in low earth orbit) and coverage for the high latitudes, as well as the rest of the globe. The European Organisation for the Exploitation of Meteorological Satellites (EUMETSAT) is in the early phase of a microsat constellation program called EPS-Sterna which would be used for operational forecasting in combination with existing meteorological programmes. The constellation would improve global NWP accuracy and provide nowcasting [3] capabilities in the arctic region with very short revisit times in the high latitudes, as well as support global efforts on climate change monitoring. The Arctic Weather Satellite (AWS) is the baseline satellite for this constellation.

### A. EXISTING CROSS-TRACK MICROWAVE SOUNDERS

EUMETSAT operates the European meteorological satellites (MetOp) in SSO used for operational forecasting and NWP. The MetOp program is about to be upgraded with a new fleet of satellites under the MetOp-second generation (MetOP-SG) mission. The operational atmospheric sounder for the MetOp-SG mission is the Microwave Sounder (MWS) instrument which is a cross-track scanning radiometer covering 5 bands (24, 50, 89, 164-183 and 229 GHz) with a total of 24 channels [4]. The MWS design is driven by a very stringent beam co-alignment requirement, which allows for easy comparison of the different bands and/or combined data products. This is achieved by overlaying individual beams

onto a single flat scan mirror using a sequence of dichroic plates, polarising grids and mirrors [5]. Dichroic plates are needed as some bands are measured in both polarisations using a separate feedhorn for each polarisation. While the data products are more easily extracted with this setup, it results in a large and complex quasi-optical setup. For the MWS this is acceptable since it is mounted on a large satellite platform (MetOP-SG Sat-A) as part of an operational suite of 8 instruments. Only one Sat-A will be in use at a time, resulting in relatively long revisit times.

The main American operational microwave radiometer is the Advanced Technology Microwave Sounder (ATMS). Like MWS, it is a cross-track radiometer operating in similar frequency bands (30, 50, 89, 164-183 GHz). However, the ATMS design is more compact compared to the MWS, partially due to lacking the 229 GHz band, but there are some key differences in the quasi-optical design as well. Instead of overlaying all beams, ATMS splits its bands into two sets each with their own flat scanning mirror [6]. The two scanning mirrors are driven by the same motor, ensuring synchronicity. Each scanning mirror then couples into their respective stationary parabolic mirror. After the parabolic mirror the two bands of the set are separated using a polarising grid, which is less lossy than a dichroic plate but limits the bands to a single polarisation. The advantage of not combining all the beams is a reduced volume compared to MWS. ATMS is part of the payload of two satellites: NOAA-20 and Suomi NPP with a third (NOAA-21) recently launched. NOAA-20 and Suomi NPP share the same SSO but are 180 degrees phase shifted, which results in better revisit times than MetOP-SG.

The Time-Resolved Observations of Precipitation structure and storm Intensity with a Constellation of Smallsats mission (TROPICS) from NASA is using similar bands, but mounts the radiometer on six dedicated cubesats in three LEO planes. The baseline median revisit time is 60 minutes in the tropics, which is needed to observe the rapidly changing cyclones occurring in this region. The TROPICS radiometer covers 4 bands (90, 118, 183, 205 GHz) with a total of 12 channels [7]. TROPICS uses very compact optics that fit in a 1U cube. By using a wideband feedhorn for the 90 and 118 GHz bands with a second feedhorn for 183 and 205 GHz bands and co-aligning them using a polarising grid, the volume of the optics is further reduced than for ATMS. Additional space saving is achieved by using a single static parabolic reflector and rotating the entire cube housing the optics. However, this severe size restriction limits TROPICS in both frequency (lower frequency horns are too big) and in available bands (1U could not accommodate more feedhorns). Unlike the previous two missions, TROPICS is a science based mission and not being used operationally for meterological forecasts [7].

The key driver for the quasi-optical design of ATMS, MWS and TROPICS is the beam alignment. Combined data products and other comparisons require measurements of the same location. Consequently, one solution is to build large and intricate quasi-optics (MWS), or limit the amount of bands (TROPICS) or a compromise between the two (ATMS). The new Arctic Weather Satellite (AWS) mission is using a different approach to this design trade-off.

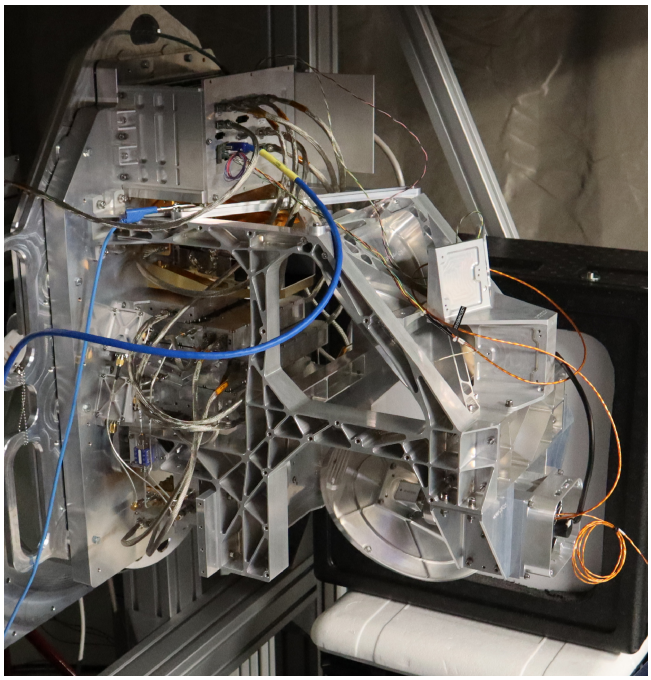

**FIGURE 1.** Picture of AWS radiometer prototype at AAC Omnisys.

### B. THE ARCTIC WEATHER SATELLITE MISSION

The AWS is a prototype for a future constellation for EUMETSAT called EPS-Sterna. The constellation consists six satellites on two SSO planes with a revisit time in the high latitudes of 60 minutes or less. Each satellite carries the same instrument: A cross-track scanning microwave radiometer covering the 50, 90, 165-183 and 325 GHz bands [8]. These four bands are split into a total of 19 channels (8, 1, 6, 4 channels from lowest to highest frequency band) which are used to extract temperature and water vapour profiles, as well as cloud liquid water content and precipitation. Including the 325 GHz band is a distinguishing addition to the AWS radiometer over the other operational radiometers. The AWS mission is intended to be a fully operational constellation used for regular forecasting and nowcasting in the arctic region and will be the first of its kind. The AWS radiometer, built by AAC Omnisys, covers its four bands (54, 89, 183, 325 GHz) with a feedhorn for each band. Due to the large number of satellites required, the AWS radiometer cannot be of the same size and complexity as the MWS, as costs would be prohibitive. Nevertheless, the radiometer performance should be similar to MWS levels to be useful operationally. Instead of overlaying the beams using dichroics or polarising grids, the feedhorns are arranged adjacent to each other in a feedcluster, directly illuminating the primary reflector (Fig. 1, 2). This significantly shortens

the path length and compacts the quasi-optics. The primary reflector is an off-axis parabolic reflector and rotates continuously to facilitate the scanning as well as calibration measurements. A secondary static reflector is located 180° from the nadir view Fig. 3. The calibration reflector covers a scanning range of 10° with a super-elliptical rim to provide sufficient measurements of the on-board calibration target (OBCT) which is positioned underneath the calibration reflector, nested inside the instrument to protect it from a direct spaceview. The OBCT consists of a wedge shaped epoxy based absorber cast on aluminium backing plates and is used as the "hot" calibration point. Cold sky measurements are used for the cold calibration point. Since the feedhorns are not co-aligned on the focal axis of the reflector, they introduce asymmetries and other imperfections in several aspects of the quasi-optical design, which will limit its performance compared to other solutions (e.g., MWS). Furthermore, the beams diverge on the ground track and measurements taken at a given moment will not be of the same location for each band. Consequently, each measurement needs to be geolocated individually so data products can be produced. Measurements will be separated in time by up to a couple of seconds, but this is not a concern as the timescales of relevant meteorological processes are much larger. For accurate geolocation and consideration of the aforementioned effects, the quasi-optics are modelled in detail so they can be accounted for in software to improve the performance of the AWS. This paper summarises the efforts of simulating and optimising the AWS quasi-optical setup, using the CHAMP and GRASP software packages from TICRA. Only the lowest, highest and middle channel for each band were simulated. For the 89 GHz band (single channel) the upper and lower bandlimits were simulated.

## II. FEEDCLUSTER DESIGN

While corrugated horns are widely used for microwave radiometers, their manufacturing is costly and complex. Circularly symmetrical horn designs in a splitblock design were chosen, which are simpler and faster to manufacturer [9]. The splitblock consists of three metal blocks, which are stacked on top of each other to form four feedhorn cavities. The plane where the faces of two blocks meet is called the splitplane and must contain the axis of symmetry for any horn it intersects, as the splitblock also contains the waveguide transition and a rectangular waveguide bend to interface with the receivers (Fig. 5). The splitplane must be located in the E-plane of the waveguide to minimise losses. However, this restricts the degrees of freedom for the horns in the splitblock, as the aperture face has to be perpendicular to the splitplane to guarantee the correct intersection.

### A. FEEDHORNS

The primary design concern for the feedhorns is the trade-off between aperture size (and thus offset to the focal axis) and directivity needed for the required footprint size. Secondly, since all horns share an aperture plane, the respective phase centers should be as close to each other as possible to prevent degraded performance of individual feedhorns. Finally the horn designs are optimised to achieve a high Gaussian coupling efficiency (95.5% and higher). Smooth walled spline horn profiles provided by Omnisys AAC were imported into CHAMP and simulated. The resulting beam patterns, which were consequently used in the GRASP simulations, are shown in Fig. 4.

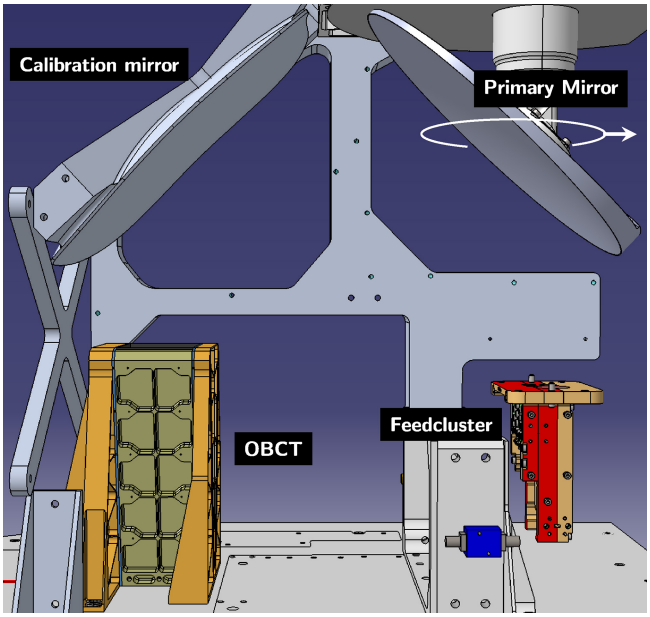


**FIGURE 2.** Overview of optical elements of the AWS radiometer. Scan plane and nadir direction indicated by white ellipse and arrow.

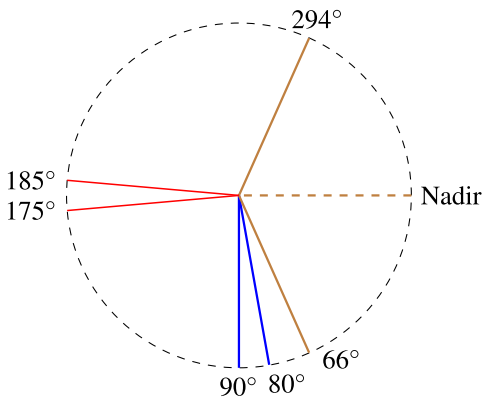


**FIGURE 3.** Scanning angle breakdown. Earth view in brown, cold sky in blue and calibration reflector in red.

### B. FEEDCLUSTER OPTIMISATION IN FOCAL PLANE

The precise packing of the feedcluster is nevertheless challenging. The final beamshape symmetry leaving the primary reflector is dictated by the distance of the horn from the focal point of the mirror in the focal plane. It is important to keep in mind that instead of absolute distance, the separation should be measured in wavelength of the respective horn, as this dictates the extent of beam distortion.

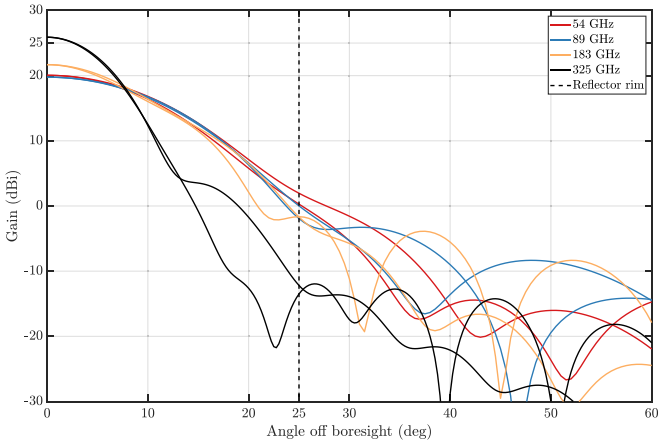


**FIGURE 4.** Antenna pattern of final feedhorns in E- and H-plane generated using CHAMP.

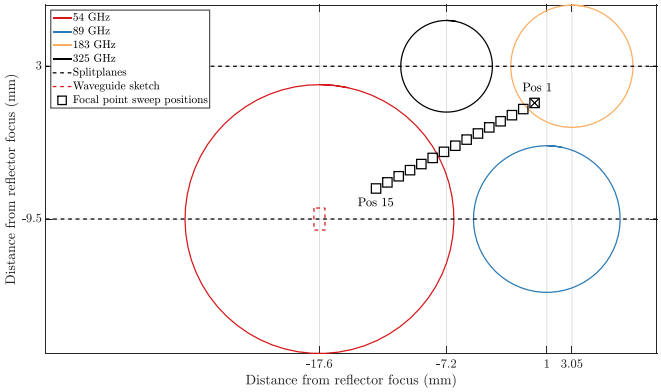


**FIGURE 5.** Plot of feedcluster and focal point sweep Positions. Waveguide sketch not to scale.

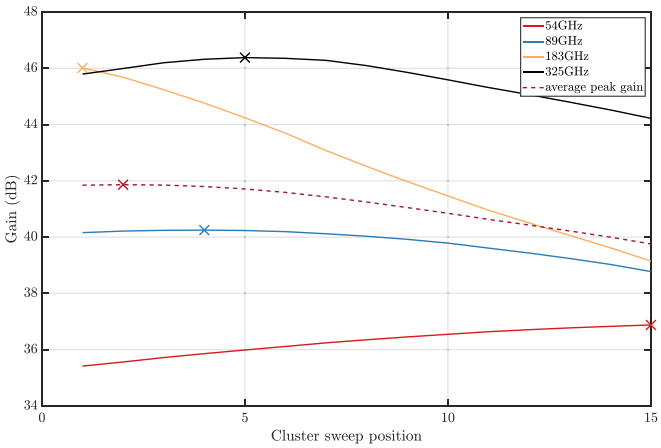


**FIGURE 6.** Peak gain in mid band in the farfield of the primary reflector as a function of focal point position.

Additionally, the effect of the beam distortion depends on the beamshape of the horn, so not all horns will be affected equally. Initially the use of iterative algorithms was considered to determine the optimal packing, but this was ultimately rejected as there was a lack of means to accurately quantify one horns relative importance over another. Furthermore, the packing problem is compounded by the fact that two feedhorns need to share a splitplane through their midpoint while they cannot extend through the splitplane of the other two feedhorns. Furthermore, the option to tilt the individual horns so they point towards the reflector was considered. This did not improve beamshape for any band, although it did reduce the spillover for the 54 GHz band by 1%. However, this spillover improvement was limited to 54 GHz and came at a cost of more divergent beam pointing. Given the added complication for the configuration of the splitplanes in the splitblock and the subsequent impact on receiver interfaces with the splitblock, tilting the feedhorns was disregarded.

Fig. 5 shows the final feedcluster packing which was used. Having decided on a packing configuration, the next step was to decide where the focal point of the reflector should be located in the aperture plane of the feedcluster. As the 183 GHz horn performance was deemed most critical the initial position of the focal point was close to its center. This position put the 54 GHz horn at the furthest wavelength number away from the focal point.

By sweeping the focal point along a straight line between the two horns centers the trade-off in performance between the 54 GHz and 183 GHz horns can be quantified. Only points on this line were considered, since it was the solution that affected the performance of the other two horns the least. Fig. 6, showing the peak gain for each horn in the farfield of the primary reflector, demonstrates the effect well. Peak gain for the 183 GHz beam decreases steadily as the focus is moved further away from it, whereas the 54 GHz beam increases as the focal point is moving closer to it, but the decline in 183 GHz is larger than the gain for the 54 GHz band. Both 89 and 325 GHz horns show a maximum gain value at the focal point which corresponds to minimum separation to the focal point. Since the gain is directly linked to the full-width half maximum (FWHM) of the beam, which in turn is specified in the radiometer's requirements, large variations are not acceptable.

Lastly, the circularity of each beam in the farfield of the primary reflector was investigated (Fig. 7). This parameter was also controlled by requirements from the end-user, placing a deviation limit from the nominal circular footprint size. Assuming a circular footprint, this deviation can be controlled using gain variations in the feedhorns. However, due to none of the horns being in focus and hence not symmetric around the focal axis, it is to be expected that beam deformation occurs.

The 89 and 325 GHz horns both show the by now familiar effect of peak values near their closest proximity position. The 183 GHz maximum circularity is also at the expected position, but its behaviours across the positions is unexpected. One would have expected a drop-off similar to 89 GHz and not a cyclical behaviour.

Averages of each parameter are also plotted in the figures to gain an appreciation of how the system changes

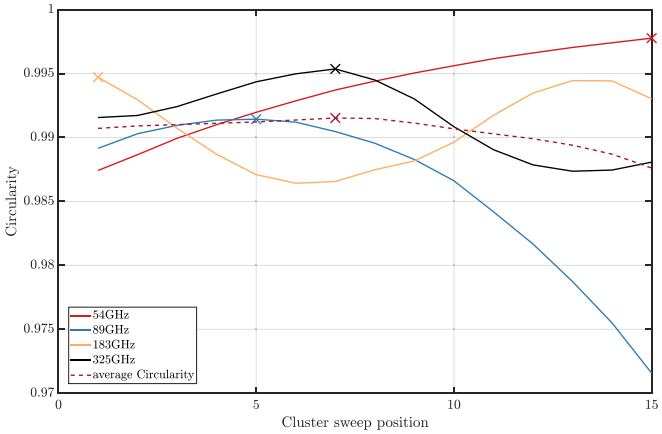


**FIGURE 7.** Circularity in mid band in the farfield of the primary reflector as a function of focal point position.

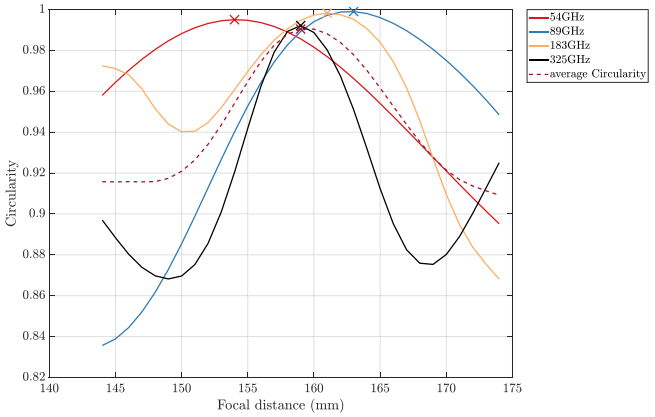


**FIGURE 8.** Farfield beam circularity as a function of distance between reflector and feedcluster.

as a whole as a function of cluster position. However, this cannot be used as a direct criteria for system performance, as certain frequency bands are more critical to the instrument and thus their performance weighs more heavily in consideration. On balance, the first sweep position was considered the most suitable since it delivers peak performance for the 183 GHz band, with minor degradation to no variation in 89 and 325 GHz. Its clear downside is the degraded performance in the 54 GHz band. Nevertheless, the 54 GHz performance was still acceptable and improving it is not worth the sacrifices in the other bands.

### C. FEEDCLUSTER OPTIMISATION ALONG FOCAL AXIS

When optimising the feedhorns, it became clear that forcing a common phase center location in each horn, while maximising other performance criteria, was too restrictive. Hence each horn as a different phase center location, along its axis of symmetry inside the horn. In order to find the optimum for the overall feedcluster, the 3dB contours of each horn in the farfield of the reflector were calculated as a function of distance to the primary reflector. The key performance criteria is the circularity of these 3dB contours and can be seen in Fig. 8. The dashed line shows the average circularity of which the peak was chosen as the focal distance for the instrument. The plot also illustrates how each horn shows a wavelength dependent drop off. The width of the peak is thinnest for 325 GHz and proceeds to get wider, as wavelength increases to 54 GHz. The final focal distance chosen was 159 mm, as it yielded the highest average circularity of the beams. The circularity was calculated using [10]:

$$\text{Circularity} = \frac{4\pi \cdot \text{Area}}{\text{Perimeter}^2} \quad (0 < \text{Circ} < 1) \qquad (1)$$

where a perfect circle has a value of 1.

## III. PRIMARY REFLECTOR

The main design challenge for the primary reflector is the large offset of the 54 GHz horn from the reflector focal point. While the gain of the 54 GHz feedhorn is matched to the reflector diameter of 160mm, the offset causes the feedhorn pattern to under-illuminate one side of the reflector and to spill past the reflector on the other side. An additional effect occurs due to the rotation of the primary reflector. As the feedhorn is offset from the axis of rotation of the reflector (its focal axis), it will lead to changes in the amount of spillover as a function of the scan angle. This occurs due to the rim of the mirror moving in the field of view of the feedhorn. If the spillover intensity varies between the calibration measurement and the earth measurement, it will produce a bias on the calibrated measurement.

The most straightforward solution would be to change the feedhorn gain to underilluminate the reflector as a whole, reducing the change in spillover due to any potential offsets. But this is not possible due to the beam footprint requirements. A second option would be to move the feedhorn closer to the primary reflector without changing its gain. While this is an option for the 54 GHz in isolation, when considering the other three feedhorns in the cluster this stops being feasible. Due to the tight packing of the horns, moving the 54 GHz horn would result in it interfering with the beams of the other horns. Consequently, the remaining option is to change the size and design of the primary reflector. While drastically increasing the size of the reflector would reduce the aforementioned issues, it is not a viable option due to mass restrictions on the spaceborne instrument. However, the rim offset of the reflector is an open parameter to change which does not adversely affect performance or other instrument requirements. Fig. 9 shows changes in spillover for one feedhorn over a 270° scan arc. Each blue plot corresponds to a specific rim offset and the red plot is the "ideal" rimshift based on the smallest standard deviation in spillover across the scan arc.

However, Fig. 9 is only useful for minimising the overall fraction of the beam power not hitting the reflector. It does not take into account where this spillover occurs around the reflector. Its the multiplication of the fraction of beam power ($F$) with the integrated intensity ($I$) of the area illuminated by the spillover that produces the error in the measurement

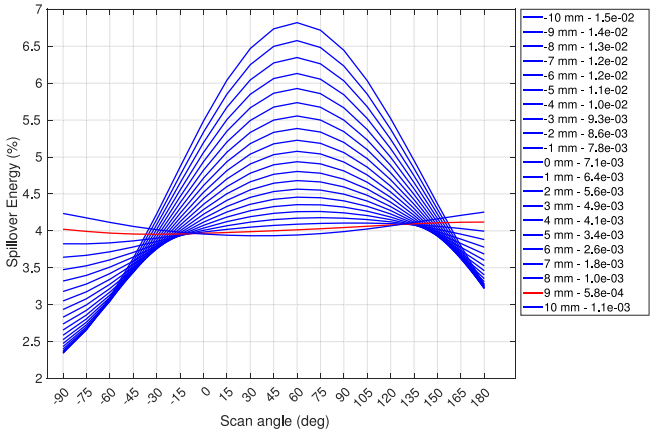


**FIGURE 9.** Spillover energy of 54 GHz horn hitting reflector across scan range as a function of rimsweep. Legend details spillover standard deviation for each rim position.

due to spillover. In equation 2, the subscript "mb" refers to the mainbeam and "i" to any arbitrary area in view of the spillover, e.g., structural elements of the satellite:

$$I_{total} = F_{mb} \cdot I_{mb} + \sum_{i=1} F_i \cdot I_i \tag{2}$$

Therefore it is possible for significant differences in spillover intensity to occur if the spillover views deep space ($\approx 3K$) for one scan angle and earth ($\approx 300K$) for another. Fig. 10 shows the total power farfield of the primary reflector for one frequency band and scan angle with specific regions of interest highlighted. As the GRASP output is saved in an Azimuth over Elevation grid where the z-axis is in line with (0,0) with poles at $\pm 90°$, each elements power value is normalised to the full sphere power $4pi$:

$$P_{normalised} = P_{element} \cdot cos(\phi) \cdot d\phi \cdot d\theta \tag{3}$$

where $\phi$ is the elevation angle which circles the pole and $d\phi, d\theta$ are the grid element sizes.

By integrating the energy fraction inside the regions of interest, the spillover can be further broken down by specific regions of interest. There is uncertainty in this approach, since the instrument's structure defining the outline of the spaceview are in the nearfield of the primary reflector. As a quality check to this approach, the sum of all the regions of interest was compared to the overall spillover of the primary reflector as reported by GRASP. The biggest difference across all tested bands and scan angles was: 0.2%. Detecting and mitigating significant spillover contributions from an earth view was the main objective, due to the earth's wide range of brightness temperatures in the atmosphere (54, 183 and 325 GHz) and also on ground (89 GHz) [11]. These variations could introduce a bias in the measurement which will depend on the instruments location above ground and the scan position of the primary reflector. This method was followed for the 54, 89 and 183 GHz band and for several scan angles (0, 66, 90, 180, 294). Since the overall spillover in the 325 GHz band is significantly lower (≈0.3%) than

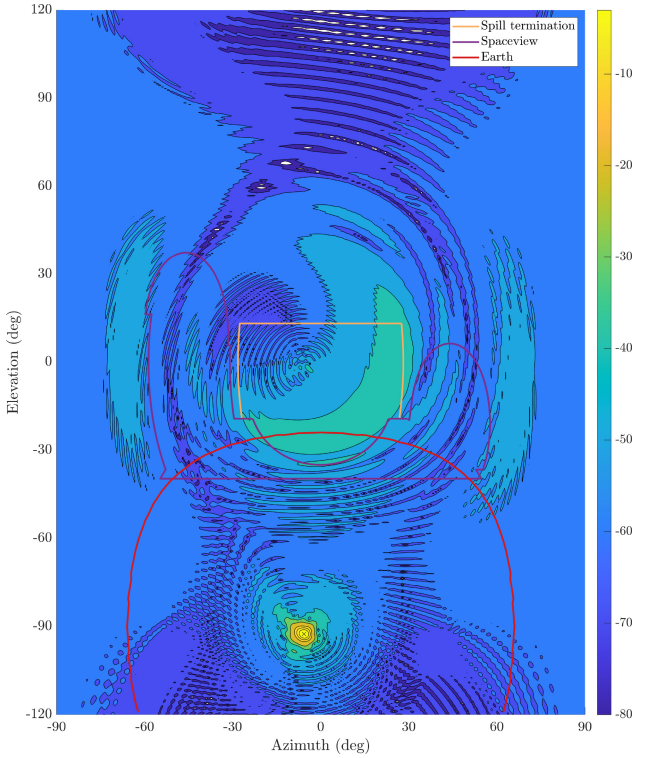


**FIGURE 10.** 54 GHz farfield from primary reflector highlighting different key features in the farfield. Origin corresponds to the flight direction of the satellite. Beam shown in nadir scan position.

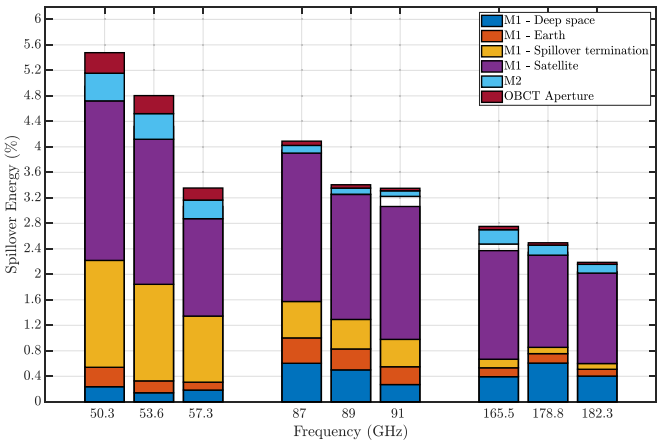


**FIGURE 11.** Spillover energy distribution for a scan angle of 180 degrees - OBCT facing. White gap between stacked bars due to mismatch of farfield integration and GRASP spillover.

for the other bands it was not considered to avoid tripling the simulation time per scan angle. The analysis showed a large spillover lobe which moved as a function of scan angle and was in view of earth. To mitigate this, the instrument design was modified to include an absorber plate behind the primary reflector which was shaped to capture this spillover lobe (marked in yellow in Fig. 10). When considering this addition, a plot summarising all spillover contributions for a given scan angle can be produced (Fig. 11).

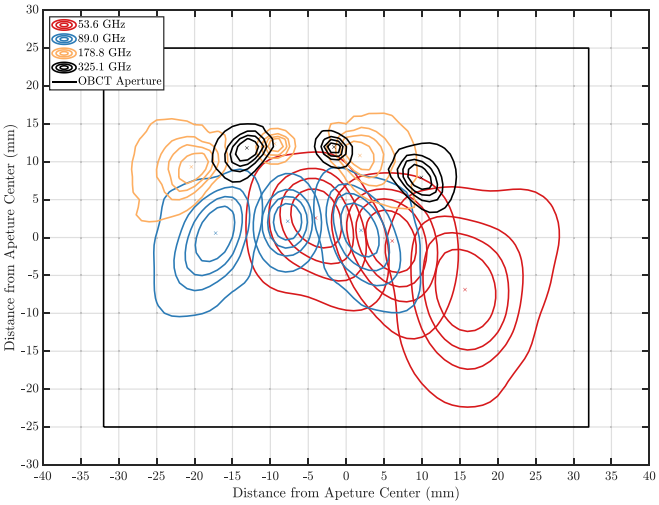


**FIGURE 12.** –3, –6, –10, –20 dB beam contours projected on OBCT aperture for 175, 180 and 185° scan angle (left to right).

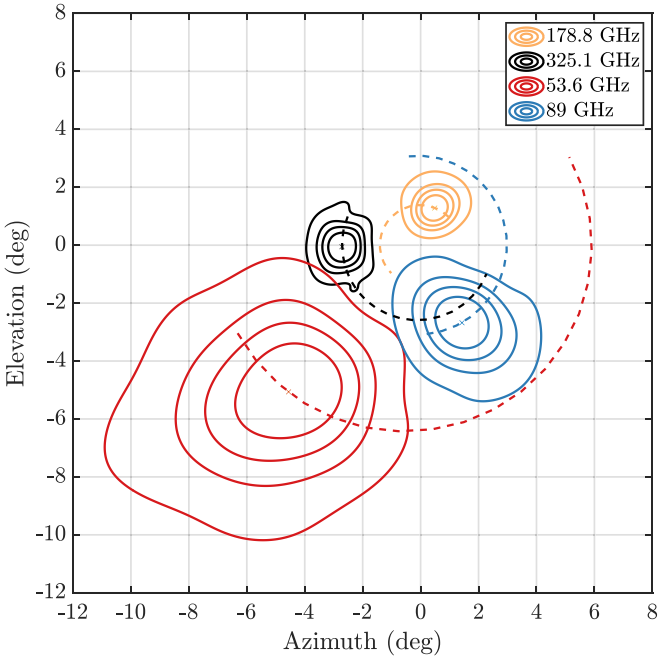


**FIGURE 13.** –3, –6, –10, –20 dB Contours of co-polar farfield AWS beams relative to the pointing vector of the primary reflector for a scan angle of 294°.

## IV. CALIBRATION REFLECTOR

The calibration reflector is a static off-axis parabolic reflector used to focus the antenna beams on the aperture of the OBCT. As the calibration reflector had to be mounted between the two main structural elements of the instrument, it was restricted in size and position. Simultaneously, it needed to cover a 10° arc of the scan range of the primary reflector. By placing it close to the primary reflector and using a super elliptical rim shape, its overall size is reduced.

The second parameter governing its size is the focal distance which is driven by the distance of the OBCT aperture to the reflector. A smaller focal distance requires a greater curvature of the reflector, resulting in more mass. The distance of the OBCT aperture in turn is driven by the wedge opening angle which is fixed at 12° for performance [12]. A larger aperture requires a deeper wedge, which decreases the distance between the reflector and aperture. To find the smallest possible wedge aperture, beam contours are plotted on a planar grid located at the focal distance of the reflector (see Fig. 12). By iterating through this process, an aperture can then be chosen that captures each beam across a 10° scanning arc. The width of the arc, rather than its absolute position in the scan cycle (Fig. 3) is important. Although the 54 GHz band is close to the edge of the aperture at a scan angle of 185°, measurements can be taken prior to 175°, where it is better captured by the aperture. However, the 54 GHz band is still the size driver, as for all other optical components. To determine the aperture spillover for each scan position it was modelled as a surface in GRASP. Along with the calibration reflector spillover, it was added to the stacked bar chart of spillover sources to form a complete picture of spillover sources (Fig. 11). The figure shows a slightly higher spillover for the calibration reflector (M2) and the OBCT aperture for the 54 GHz compared to the other bands.

## V. FARFIELD PERFORMANCE

Taking into account the optimisation detailed in the previous sections, Fig. 13 shows the co-polar farfield beams for each band, relative to the pointing vector of the primary reflector (plot origin). A beam sitting in the focal point of the primary reflector would have its beam center on the origin. However, due each beam's offset from the focal point, they are diverging in the farfield. The angular distance from the origin in the farfield is directly related to the offset of the horn in the feedcluster (Fig. 4). Thus, the 54GHz is the furthest away from the origin. However, this relative offset position is scan angle dependent. The dashed line plots the movement of the corresponding beam center as a function of scan angle from 270° to 90° encompassing the relevant scan angles for earth scanning and cold sky measurements. The beam movement is circular with a fixed radius around the pointing vector. This scan angle dependent movement needs to be accounted for when geo-locating the individual beams, but is fully characterised from the GRASP simulations. It is also evident in Fig. 12 over the 10° arc and accounted for in the OBCT aperture sizing.

The beam contours also exhibit a variation as a function of scan angle. This farfield variation increases with horn offset from the focal point of the reflector. When defining the mainbeam contour, one needs to consider both the fundamental ellipticity of the farfield beam and its variation. While determining the actual beam contour for each channel for each scan angle is possible, this is computationally too expensive for operational processing. Instead, an ellipse is fitted to the −3dB mid band contour of each horn and scaled up by a factor of 2.5. In post processing the length of the

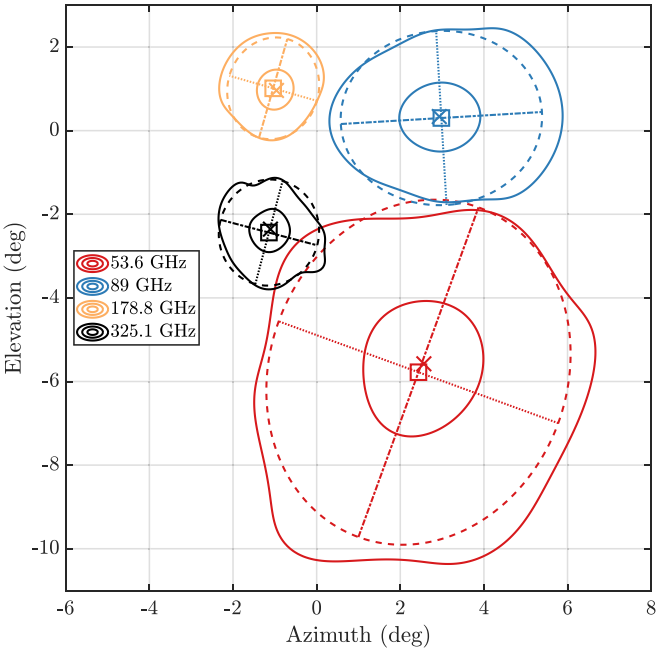


**FIGURE 14.** −3, −20 dB co-polar beam contours vs fitted mainbeam ellipse for a scan angle of 0° (nadir). Solid lines are simulated contours. Dashed lines are elliptical approximations. Dotted and dash-dotted lines are minor and major axes of the ellipses. Boxes mark the center of the ellipse and crosses the peak gain of the simulated contour.

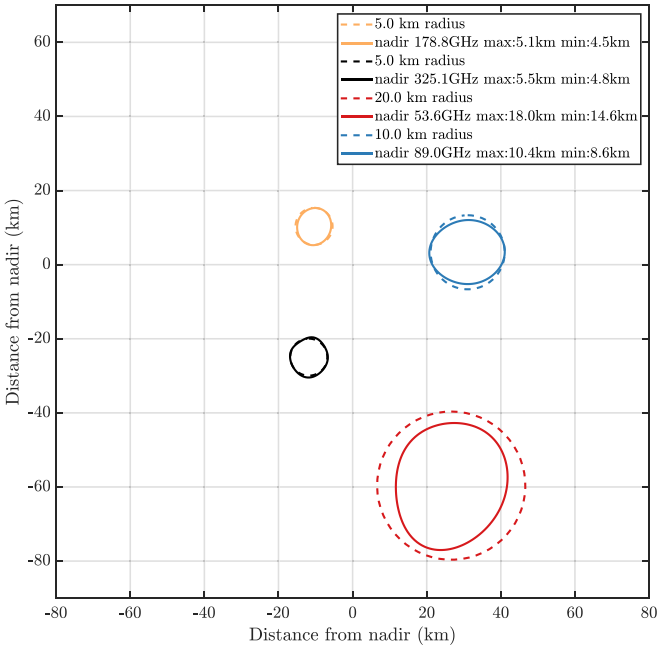


**FIGURE 15.** Full width half maximum footprints of actual AWS beams projected on ground vs maximum footprint requirements for nadir scan angle.

semi-major and semi-minor axes of the fitted ellipse along with their scan angle dependent orientation to the origin can then be used to define a mainbeam. Fig. 14 demonstrates this approach for a nadir (0°) scan angle. It also serves as an example of the scan dependent variations when comparing the contours to Fig. 13.

Two mainbeam efficiency definitions were considered during the design of the optics, both using the elliptical approximation of the mainbeam, but differing in the definition of the total power used:

$$mbe = \frac{P_{ellipse}}{P_{farfield}} \tag{4}$$

$$mbe = \frac{P_{ellipse}}{4 \cdot \pi} \tag{5}$$

Using (4), only the total power in the simulated farfield (30° x 30° grid) is considered and assumed to be 100%. Since AWS is calibrated via the main reflector, this definition is justified, if the spillover is constant for all scan angles and therefore does not affect calibration. However, (5) is required when spillover of the reflector and far sidelobes should be considered, which scales the mainbeam power by the total power radiated from the feedhorn.

While the ellipticity of the beams is a natural consequence of the instrument design, trade-off decisions were made to increase circularity for one band at the sacrifice of another. Evaluation of trade-offs is driven by the mission requirement on footprint size and allowable deviation. Fig. 15 shows the −3dB contours projected on ground in nadir in comparison to the maximum footprint size defined in the mission requirements. Each nominal maximum radius is given with a tolerance of ±25%. While the overall footprint size is driven by the horn and primary reflector, the ellipticity induced by the optics on the footprint may not infringe on these limits. Table 1 shows a summary of the farfield performance for all simulated frequencies.

## VI. SUMMARY

The AWS mission is a prototype for the EPS-Sterna constellation consisting of a constellation of six satellites on two sun-synchronous orbital planes, which will improve global NWP in combination with the existing Met-OP and NOAA programmes. Furthermore it will increase the frequency of measurements in the high latitudes and achieve operational nowcasting capability in the arctic region. Each satellite will carry a single identical payload; A four band (54, 89, 183, 325 GHz) radiometer built by AAC Omnisys. Due to the large number of radiometers that are required for this mission they need to be smaller and less complex than previous operational radiometers (MWS, ATMS), but achieve similar performance. The AWS radiometer achieves this by using a feedcluster in a splitblock directly illuminating the primary (scanning) reflector, foregoing the need for other optical elements for beam co-alignment. The feedcluster contains four smooth-walled spline horns. As no horn is in focus of the primary reflector, this design decision results in asymmetries and scan angle dependent performance variations. Using the GRASP and CHAMP software from TICRA, the quasi-optics of the radiometer were simulated and optimised. Performance trade-offs were made during optimisation of the feedcluster configuration and positioning, maximising beam circularity and gain. The primary and calibration reflectors

**TABLE 1.** Performance summary in nadir for all simulated frequencies. Beam centers stated relative to pointing of primary reflector. Footprints stated as minor and major radius of ellipse. Mainbeam efficiencies stated for equation (4) without brackets and equation (5) in brackets.

| Frequency | Beam center (nadir) | FWHM footprint | Mainbeam efficiency |
|---|---|---|---|
| 50.3 GHz | x: 2.55° | 15.2 km | 96.4% (91.9%) |
| | y: -5.67° | 18.5 km | |
| 53.6 GHz | x: 2.54° | 14.6 km | 96.6% (92.7%) |
| | y: -5.68° | 18.0 km | |
| 57.3 GHz | x: 2.49° | 14.2 km | 96.9% (94.2%) |
| | y: -5.71° | 17.4 km | |
| 87.0 GHz | x: 2.96° | 9.1 km | 96.7% (93.0%) |
| | y: 0.32° | 10.4 km | |
| 89.0 GHz | x: 2.96° | 8.6 km | 96.8% (93.7%) |
| | y: 0.32° | 10.4 km | |
| 91.0 GHz | x: 2.95° | 8.9 km | 96.8% (93.8%) |
| | y: 0.32° | 10.0 km | |
| 165.5 GHz | x: -0.99° | 4.7 km | 96.4% (94.0%) |
| | y: 0.99° | 5.5 km | |
| 178.8 GHz | x: -0.99° | 4.5 km | 96.8% (94.6%) |
| | y: 0.99° | 5.1 km | |
| 182.3 GHz | x: -0.99° | 4.5 km | 96.6% (94.7%) |
| | y: 0.99° | 5.1 km | |
| 321.8 GHz | x: -1.13° | 4.9 km | 98.0% (97.7%) |
| | y: -2.38° | 5.5 km | |
| 325.1 GHz | x: -1.13° | 4.8 km | 98.0% (97.7%) |
| | y: -2.38° | 5.5 km | |
| 328.5 GHz | x: -1.13° | 4.8 km | 97.9% (97.6%) |
| | y: -2.38° | 5.6 km | |

were optimised to minimise overall spillover and its scan angle dependency. Farfield beam divergence, beam shape, beam pointing and their scan angle dependency was also simulated. Furthermore, a simple method of mainbeam definition for the elliptical beamshapes was detailed.

## REFERENCES


[1] N. Bormann, H. Lawrence, and J. Farnan. "Global observing system experiments in the ECMWF assimilation system." Sep. 2019. [Online]. Available: https://www.ecmwf.int/node/18859

[2] K. Lean, N. Bormann, S. Healy, and S. English. "Final report: Study to assess earth observation with small satellites and their prospects for future global numerical weather prediction." Feb. 2022. [Online]. Available: https://status.ecmwf.int/en/elibrary/81324-final-report-study-assess-earth-observation-small-satellites-and-their-prospects

[3] Y. Wang et al., *Guidelines for Nowcasting Techniques*, World Meteorl. Org., Geneva, Switzerland, Nov. 2017.

[4] V. Kangas et al., "Microwave sounder instrument for MetOp second generation," in *Proc. 13th Specialist Meeting Microw. Radiometry Remote Sens. Environ. (MicroRad)*, 2014, pp. 232–235. [Online]. Available: https://ieeexplore.ieee.org/document/6878947

[5] R. Wylde. "MWS QON delivered to airbus U.K." 2018. [Online]. Available: http://terahertz.co.uk/news/mws-qon-delivered-to-airbus-uk

[6] C. Muth, P. Lee, J. Shiue, and W. A. Webb, "Advanced technology microwave sounder on NPOESS and NPP," in *Proc. IEEE Int. Geosci. Remote Sens. Symp. (IGARSS)*, vol. 4, 2004, pp. 2454–2458.

[7] W. J. Blackwell et al., "An overview of the TROPICS NASA earth venture mission," *Quart. J. Roy. Meteorol. Soc.*, vol. 144, no. S1, pp. 16–26, 2018. [Online]. Available: https://rmets.onlinelibrary.wiley.com/doi/abs/10.1002/qj.3290

[8] B. Lagaune, S. Berge, and A. Emrich, "Arctic weather satellite, a microsatellite constellation for improved weather forecasting in arctic and globally," in *Proc. 35th Annu. Small Satellite Conf.*, 2021, p. 2. [Online]. Available: https://digitalcommons.usu.edu/cgi/viewcontent.cgi?article=5087&context=smallsat

[9] A. Hammar et al., "THz smooth-walled spline horn antennas: Design, manufacturing and measurements," in *Proc. IEEE Int. Symp. Antennas Propag. (APSURSI)*, 2016, pp. 1341–1342.

[10] E. P. Cox, "A method of assigning numerical and percentage values to the degree of roundness of sand grains," *J. Paleontol.*, vol. 1, no. 3, pp. 179–183, 1927. [Online]. Available: http://www.jstor.org/stable/1298056

[11] F. Ulaby et al., *Microwave Radar and Radiometric Remote Sensing*. Ann Arbor, MI, USA: Univ. Michigan Press, Jan. 2014, ch. 8, pp. 317–328.

[12] K. Jacob, A. Schröder, and A. Murk, "Design, manufacturing, and characterization of conical blackbody targets with optimized profile," *IEEE Trans. THz Sci. Technol.*, vol. 8, no. 1, pp. 76–84, Jan. 2018.


**ROLAND ALBERS** received the B.Eng. degree in aerospace engineering from Brunel University, London, in 2015, and the M.Sc. degree in astronautics and space engineering from Cranfield University, Milton Keynes, in 2016. After working in the space industry on quasi-optical components, he is currently pursuing the Ph.D. degree in applied physics with the University of Bern, Switzerland. His research interests are spaceborne radiometry, hardware design, and calibration.

**ANDERS EMRICH** received the M.Sc. and Ph.D. degrees in electrical engineering from the Chalmers University of Technology, Göteborg, Sweden, in 1985 and 1992, respectively. In 1992, together with S. Andersson, he founded Omnisys Instruments AB, Västra Frölunda, Sweden, and was responsible for several subsystems for the ODIN radiometer payload and many development contracts toward ESA/ESTEC. He has been engaged in research collaborations with the Chalmers University of Technology and other research institutes and universities for more than 30 years. He has a Co-Supervisor for three Ph.D. students at Chalmers. He has been responsible for the design, development, and production of the 183-GHz Water Vapor Radiometer (58 units) for ALMA, the GAS radio interferometer demonstrator (ESA contract), and the STEAMR instrument. He proposed the Artic Weather Satellite project to end users, including Eumetsat, and the Swedish National Space Agency proposed to the development project the ESA council 2019. He is currently leading the design and development of the instrument and several subsystems.

**AXEL MURK** received the M.Sc. degree in physics from the Technical University of Munich, Munich, Germany, in 1995, and the Ph.D. degree in physics from the University of Bern, Bern, Switzerland, in 1999. Since then, he has been involved in the development and characterization of millimeter- and submillimeter-wave instrumentation for different ground-based and space-borne projects. Since 2018, he has been leading the IAP Microwave Physics Division, University of Bern. His research interests include digital real-time spectrometers and the radiometric calibration of remote sensing instruments.